ARCHIVE OF MECHANICAL ENGINEERING

DOI: 10.24425/ame.2025.155872 2025, Vol. 72, No. 4, pp. 765–793

Baihang WANG [1], Heyu SHI [1], Jizu SHI [2], Xue ZHAO [3],
Tong TONG [4], Jiajun WANG [5]

# Research on real-time kinematics algorithm and gait planning of rope-driven skating training robot

**Received** 13 April 2025, **Revised** 5 September 2025, **Accepted** 16 September 2025, **Published online** 11 December 2025

**Keywords:** skating training robot, rope parallel mechanism, optical motion capture, gait planning experiment, interval analysis

The mechanism of human lower limb skating is analyzed, and the skating information is collected by optical motion capture experiment to obtain the skating trajectory of lower limb target. Aiming at the target skating trajectory and gait motion characteristics, a new type of rope-driven skating training robot configuration based on rope parallel mechanism is proposed. The kinematics analysis of the configuration is carried out, and the motion mapping relationship between the rope and the end moving platform is established. Based on interval analysis and Levenberg-Marquardt iterative solver, a real-time forward kinematics algorithm is proposed to evaluate the real-time performance and convergence performance of the algorithm. The prototype experimental platform is built and the gait planning control experiment is carried out. The experimental results show that the displacement of the moving platform in the $x$ direction, $y$ direction and $z$ direction and the rotation angle tracking of the sagittal plane and coronal plane are good. The movement error is controlled within 6mm, the rotation error is controlled at about 3°, and the lag time is about 0.23 s. The correctness of the theoretical analysis of real-time kinematics and the practicability of the algorithm are verified, which lays a foundation for further optimization of the control system.

---

✉ Heyu SHI, email: 67C10806126@udru.ac.th
[1] Udon Thani Rajabhat University, Udon Thani 41000, Thailand
[2] Jilin Institute of Physical Education, Changchun, China
[3] Changchun Jingyue High-tech Industrial Development Zone Huize School, Changchun, China
[4] Changchun Normal University, Changchun, China
[5] Heilongjiang Taiqi Tertiary Education Training Institute Co. Ltd, Harbin, China

## 1. Introduction

With the successful holding of the Beijing Winter Olympic Games, ice and snow sports have attracted wide attention around the world, and ice and snow sports have shown a vigorous development trend [1]. At the same time, the problem of the shortage of ice professional and technical personnel has also been revealed. The shortage of limited professional and technical personnel will limit the development of skating nationwide [2]. With the rise of artificial intelligence technology represented by deep learning, there appears a trend for robots to replace human work in a non-institutional environment. Skating training robot [3] is a kind of special robot which can simulate the skills of human ice and snow sports in the ice surface environment and promote its own movement with the help of low friction environmental characteristics. It has the advantages of 7×24 hours ‘on-the-job’, sinking the action analysis ability of professional athletes to colleges and universities, ice rinks and even commercial gyms, and alleviating the ‘coach shortage’ [4]. Unfortunately, there is still a lack of systematic discussion on the mechanism design, dynamic modeling and intelligent control of the robot system in the ice and snow sports scene, and the related theory and technical system are still blank [5]. Therefore, the research on the basic theory and key structure of skating training robot can not only provide new tools for the interpretation of sports injury mechanism and the optimization of training equipment, but also open up a new path for the design of a new generation of high-performance bionic robot, which has important scientific value and engineering significance [6–8].

The skating training robot is a device that uses robot technology to provide skating training for skating enthusiasts. It can simulate the skating gait of normal people and help them improve their skating ability. At present, the research mainstream of the auxiliary training robot is the exoskeleton rigid connecting rod structure, but as a rigid connecting rod mechanism, the exoskeleton auxiliary training robot inevitably has some defects: due to the design of its own rigid structure, the driving motor and the corresponding deceleration device need to be placed near each rotating joint, and the inertia of the exoskeleton connecting rod itself is added. Finally, the burden of the trainees is greatly increased, and the overall structure is more complex [9]; the sudden change in the speed of a rigid exoskeleton robot during start-stop will produce a huge inertial force, which will affect the limbs of skating enthusiasts and may cause damage to them. In addition, due to the serial link structure of the exoskeleton assisted training robot, the end trajectory error will accumulate and amplify with the series of each joint, which will affect the accuracy and performance of the exoskeleton skating training robot [10].

Compared with the exoskeleton rigid connecting rod structure, the rope drive has many advantages: the rope directly acts on the end moving platform on the body segment, and the drive device is separated from the user, which will not add additional inertia and weight to the user; the rope itself has efficient force conduction and good flexibility. By changing the force field strategy of the end moving platform, the end position is affected, which can adapt to the motion mode under different training strategies, and can effectively avoid the collision and impact of the rigid body structure in the driving process. The cable parallel mechanism has a large working space, strong bearing capacity and superior dynamic performance. It can achieve accurate trajectory tracking and force transmission, avoid the cumulative error that the series mechanism may produce, and ensure the control accuracy [11]. Many scholars have done a lot of research on the rope drive mechanism. In Reference [12], the National Institute of Standards and Technology developed the ROBOCRANE, which is considered to be the world's first wire-driven parallel robot. The de-sign of ROBOCRANE is inspired by the structure of the famous Stewart-Gough platform, which can be seen as reversing the arrangement of the Stewart-Gough platform up and down, and replacing the telescopic rod with a rope. The ROBOCRANE is used for the assembly and hoisting of large-size objects. Reference [13] proposed a rope-driven lower limb re-habilitation robot, which is composed of a rigid connecting rod and a rope drive, and changes the direction of force through a pulley group. This structure can meet the movement of the sagittal plane of the human leg, but due to the particularity of the structure, it cannot completely guide the human leg to complete the movement in the space. In [14], the Spidercam cable-driven parallel robot developed in Germany as the end-effector of the camera robot provides a very successful solution for large-area overlooking shooting.

Therefore, based on the problems existing in the exoskeleton-assisted training robot and the advantages of the rope parallel mechanism, a new type of rope-driven skating training robot is proposed. The rope is used to replace the exoskeleton rigid connecting rod as the transmission part, and the end moving platform is set in the lower limb thigh section of the participant to form the rope-end moving platform parallel mechanism, and the kinematics theory of the structure is studied. In addition, a forward kinematics algorithm combining interval analysis with Levenberg-Marquardt iterative solver is proposed to evaluate the convergence ability and real-time performance of the algorithm. The correct-ness of the theoretical analysis of the algorithm is verified.

## 2. Skating mechanism analysis and motion capture experiment

In order to determine the overall mechanism design of the rope-driven skating training robot, first of all, it is necessary to analyze the skating mechanism of the human lower limbs and understand the coordinated motion law of the lower limb joints during skating. On this basis, a configuration that conforms to the gait motion characteristics of the human body is proposed.

### 2.1. Mechanism analysis of skiing

When analyzing the mechanism of human lower limb skating, in order to accurately describe its movement, it is necessary to establish a human body space coordinate system, as shown in Fig. 1. The skating of the human body is mainly completed by the cooperation of the hip joint, knee joint, ankle joint, thigh, calf and foot of the lower limbs. Although skiing is completed by the whole lower limbs, it is mainly performed through the muscles of the thighs. The strength of the thighs can drive the movements of the calves and feet, so as to achieve sliding. It can be seen that the thigh plays a vital role in skating. The thigh moves around the hip joint through muscles. The hip joint rotates very little in the horizontal plane of the basic section of the human body, mainly completing the rotation of the joint in the coronal and sagittal planes. Therefore, the simplified hip joint has two rotational degrees of freedom around the center of the joint when the athlete is skating.

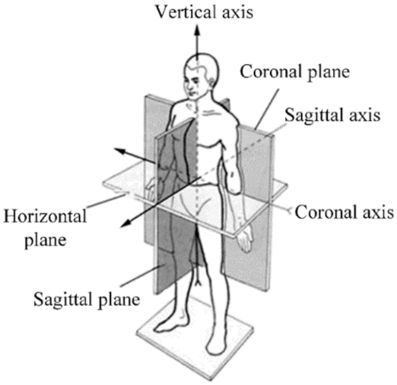

Fig. 1. Basic section of human body

## 2.2. Optical motion capture experiment

In order to obtain the movement angle of the skater's thigh along the coronal and sagittal planes, an optical motion capture experiment was carried out. The basic information of the volunteers selected is shown in Table 1. The equipment used in the experiment is NOKOV three-dimensional optical motion capture system. The laboratory is shown in Fig. 2, and the collected reflective marker points are shown in Fig. 3. The system accurately collects the spatial coordinates of the reflective Marker points during the movement through the NOKOV Mars4 H camera. This experiment is based on this principle, tracking the Marker points pasted on the volunteer's leg to complete the leg motion optical motion capture experiment. Before the experiment, 14 Marker balls were pasted on the left and right lower

Table 1. Basic information of volunteers

| Sexuality | Age [years] | Weight [kg] | Height [cm] | Thigh length [cm] | Calf length [cm] | Foot height [cm] |
|---|---|---|---|---|---|---|
| males | 25 | 75 | 180 | 56 | 44 | 10 |

limbs of the volunteers, and 3 Marker balls were pasted on the waist. Taking the right leg as an example, Marker has 1 hip and knee joint, 1 thigh and calf geometric center, 1 foot surface and 2 ankle joints.

Fig. 2. NOKOV three-dimensional optical motion capture laboratory

Fig. 3. Marker points

After the completion of the Marker point setting, the volunteers were guided to put their hands on their chests and walk freely for a period of time to adapt to the environment. After the volunteers walked stably, they were guided to perform standard skating movements, and the experimental observation and data collection were carried out through the seeker software. If the Marker point was lost, the data collection needed to be re-collected; if complete, the 17 Marker points were connected in turn, and finally the lower limb bone model was drawn, and the kinematic data of the 17 Marker points were derived. The simplified model of the volunteer's lower limb human body is shown in Fig. 4.

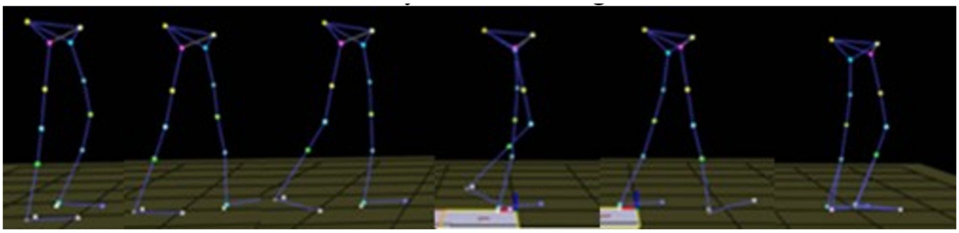

Fig. 4. The simplified model of the volunteer's lower limb human body

Because the system is to capture the three-dimensional coordinates of each Marker point under each frame, the motion and environmental factors of the volunteers during the acquisition process will cause the jitter of the Marker point, so that the captured trajectory is not smooth. Therefore, the collected hip rotation angle data needs to be smoothed. Because the human body is symmetrically distributed, the two legs move alternately during roller skating, and the motion parameters are basically the same, so it is only necessary to analyze the single leg. Let's take the volunteer's right leg analysis as an example. Through MATLAB processing data, the rotation range of the thigh along the sagittal plane during the normal training of the volunteers was $-50^\circ \div 40^\circ$, and the rotation range of the thigh along the coronal plane was $0^\circ \div 30^\circ$.

## 3. Design of rope traction skating training robot body

### 3.1. The overall structure of rope-driven skating training robot

Through the above analysis of the basic section of the skating human body and the results of the motion capture experiment, it can be seen that the skating training robot should focus on the auxiliary training of the lower limbs of the skaters. It is necessary to coordinate and cooperate with the robot to complete the action training. Therefore, when designing a rope-driven skating training robot, its structural design should follow the principles of meeting training requirements, safety and comfort, and practicality. The overall mechanism of the skating training robot designed according to the above principles is shown in Fig. 5. The skating robot is mainly composed of 1 – column, 2 – column beam, 3 – pulley, 4 – arm, 5 – calf strap, 6 – servo drive, 7 – chassis cover plate, 8 – chassis, 9 – mirror surface and rope. The column and the column beam are respectively distributed with pulleys that change the direction of the rope. The armrests on both sides of the arms are used for athletes to maintain balance during training. The mirror surface is a competition venue similar to that of athletes. The driving mode of the robot is driven by the servo motor driving the rope.

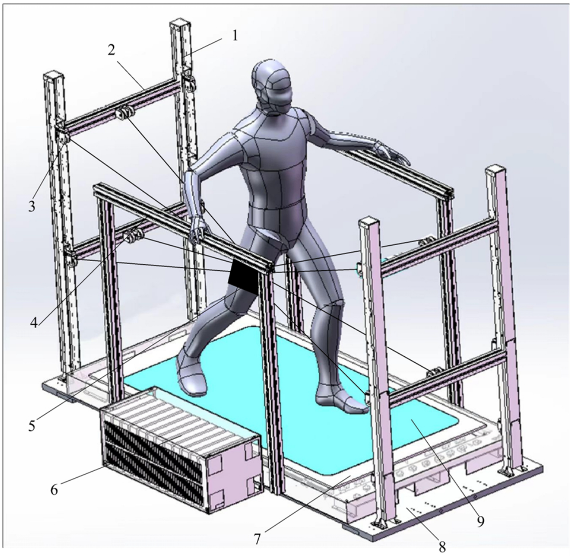

Fig. 5. Structure diagram of skating training robot: 1 – column; 2 – column crossbeam; 3 – pulley; 4 – handrails; 5 – calf strap; 6 – servo driver; 7 – chassis cover version; 8 – chassis; 9 – mirror surface

The chassis structure is shown in Fig. 6. The chassis is the basis of the rope-driven skating training robot. The chassis consists of 1 – bearing plate, 2 – slider, 3 – coupling, 4 – chassis, 5 – support plate (long), 6 – steering wheel pillar stage, 7 – support plate (short), 8 – servo single machine, 9 – ball screw and 10 – steering wheel. The chassis covered by the cover plate is equipped with 16 drive motors, 16 ball screws, 4 support plates, and 4 steering wheel struts. Four small pillars are installed on each steering wheel pillar table, and the steering wheel is installed on the small pillar to change the direction of the rope.

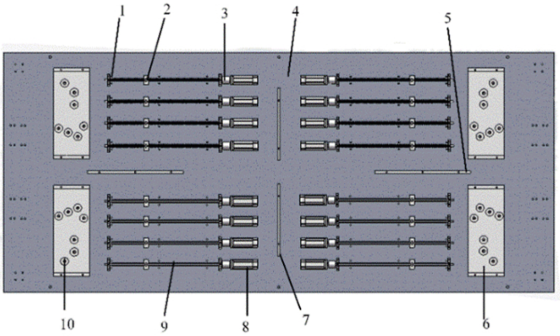

Fig. 6. Overall structure of chassis: 1 – bearing piece; 2 – slider; 3 – coupling; 4 – chassis; 5 – support plate (long); 6 – steering wheel pillar t bench; 7 – support plate (short); 8 – servo single machine; 9 – ball screw; 10 – steering wheel

The driving unit is composed of S7-1200 PLC, V90-PTI servo motor and supporting 1204 ball screw, as shown in Fig. 7. Taking the unilateral lower limb as an example, the end moving platform on the user's thigh is driven by four groups of driving units before and after, respectively, to realize the flexion and extension movement of the hip joint in the sagittal and coronal planes.

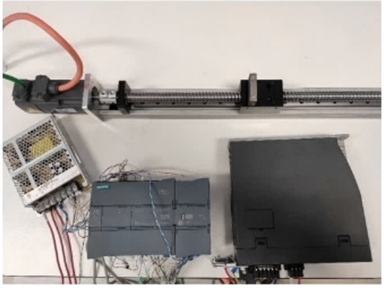

Fig. 7. Driving unit

Usually, the driving motor of the robot is generally installed at the joint position of the mechanism. This installation method causes the joint position quality to increase, which limits the motion performance of the robot. Therefore, the driving motor of the rope-driven skating training robot is installed in the position of the robot chassis, and the components directly connected to the human body are lighter, which improves the flexibility of the movement and the effect of skating training. The drive motor is connected to the ball screw through the coupling, and the rope is connected to the slider. As the motor rotates, the ball screw is driven, so that the slider moves, thereby achieving the purpose of controlling the length change of the rope and the change of the tension.

### 3.2. Establishment of geometric model

Some parameters of the rope-driven skating training robot proposed in this paper are shown in Table 2. Considering the different height and lower limb joint angle of the athletes, the physiological parameters of the lower limbs of the selected volunteers are: thigh length 560 mm, calf length 440 mm, foot height 100 mm. According to the dynamic capture experiment, the rotation range of the thigh along the sagittal plane (positive rotation in the $X$ direction) is $-50^\circ \div 40^\circ$, and the rotation range of the thigh along the coronal plane (positive rotation in the $Y$ direction) is $0^\circ \div 30^\circ$.

Table 2. Some parameters of rope traction skating training robot

| Geometric parameter | Numerical value |
|---|---|
| Height of $A_1$, $A_2$, $A_3$, $A_4$ | 1120 mm |
| Height of $A_5$, $A_6$, $A_7$, $A_8$ | 520 mm |
| Size of thigh moving platform | $300 \times 200 \times 200$ mm |
| Base size | $2000 \times 1000 \times 50$ mm |

The mechanism diagram of the skating training robot is shown in Fig. 8. The fixed coordinate system $O$-$XYZ$ and the moving coordinate system $p$-$xyz$ of the mechanism are established respectively. The fixed coordinate system is located at the geometric center of the plane $A_5A_6A_7A_8$, $O$ is the origin of the fixed coordinate system, the $Z$ axis is perpendicular to the plane $A_5A_6A_7A_8$, the $X$ axis is parallel to the $A_5A_6$, and the $Y$ axis is determined by the right hand rule.

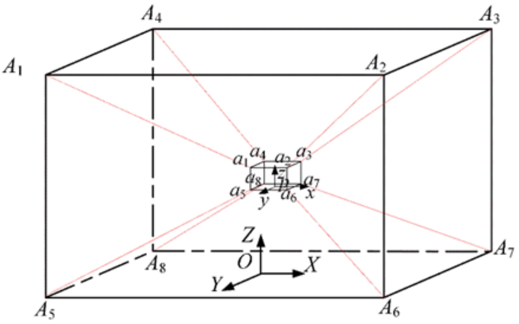

Fig. 8. Mechanism diagram of skating training robot

The moving coordinate system is located at the geometric center of the lower surface of the mobile platform. $p$ is the origin of the moving coordinate system. The $z$-axis is perpendicular to the plane $a_5a_6a_7a_8$, the $x$-axis is parallel to the $a_5a_6$, and the $y$-axis is determined according to the right-hand rule. $\boldsymbol{A}_i$ $(i = 1, 2, \ldots, 8)$ is the connection point between the rope and the static platform, and $\boldsymbol{a}_i$ $(i = 1, 2, \ldots, 8)$ is the connection point between the rope and the moving platform. Let ${}^{O}\boldsymbol{A}_i$ be the position vector of $\boldsymbol{A}_i$ in the fixed coordinate system and ${}^{p}\boldsymbol{a}_i$ be the position vector of $\boldsymbol{a}_i$ in the moving coordinate system. $\boldsymbol{L}_i = \overrightarrow{\boldsymbol{A}_i\boldsymbol{a}_i}$ $(i = 1, 2, \ldots, 8)$ is the rope vector, $\boldsymbol{l}_i$ represents the length of the rope, $2e$, $2f$, $2j$ are the length, width and height of the mobile platform, respectively. In the next analysis process, the rope is always in a state of tension, and the influence of rope elasticity and gravity is not considered.

### 3.3. Degree of freedom analysis

The degree of freedom of the robot is an important technical index of the robot performance, and it is essential to analyze the degree of freedom of the mechanism. The driving rope of the rope-driven skating training robot studied in this paper is rigid after tensioning, and in a sense, the function of the motion pair can be realized. Each driving rope can be equivalent to a branch chain with a ball pair at one end, a ball pin pair at the other end and a moving pair in the middle.

The degree of freedom of the above structure is analyzed by Kutzbach-Grübler formula [15]:

$$F = 6(N - g - 1) + \sum_{i=1}^{g} f_i\,. \tag{1}$$

Here:

$F$ – the number of degrees of freedom of the mechanism;

$N$ – the total number of components of mechanism;

$g$ – number of motion pairs;

$f_i$ – the number of relative degrees of freedom of the $i$-th motion pair.

It can be seen from Fig. 8 that the number of components of the mechanism is 18, the number of kinematic pairs is 24, and the total number of degrees of freedom is 48. The number of degrees of freedom of the mechanism can be calculated by equation (1):

$$F = 6(18 - 24 - 1) + 48. \tag{2}$$

Through the above formula, the degree of freedom of the rope-driven skating training robot is 6. It can be seen that the rotation and movement of the moving platform in three-dimensional space can be realized under the driving of 8 ropes, and the training task of skaters can be realized.

## 4. Kinematics analysis of skating training robot

### 4.1. Inverse kinematics analysis

During the movement of the rope drive mechanism, the angle of the lower limb hip joint and the length of the rope are constantly changing. Therefore, the forward and inverse kinematics solutions need to analyze the relationship between the lower limb joint angle and the rope length. It can be seen from the above that the thigh length is $L$; the length of the rope is $\boldsymbol{L}_i = \boldsymbol{A}_i\boldsymbol{a}_i$ $(i = 1, 2, \ldots, 8)$, $\boldsymbol{A}_i\boldsymbol{a}_i$ is the driving rope; the length of $a_1a_2$, $a_3a_4$, $a_3a_4$ and $a_7a_8$ is the same as $2e$; the length of $a_1a_4$, $a_2a_3$, $a_5a_8$, $a_6a_7$ is the same as $2f$; the length of $a_1a_5$, $a_4a_8$, $a_2a_6$, $a_3a_7$ is the same as $2j$; $\beta$ and $\alpha$ are the rotation angles of the hip joint around the sagittal plane and the coronal plane, respectively, and the angle of the hip joint around the horizontal plane is 0.

In the rope drive mechanism, the fixed coordinate system of the lower limb is set as $O$-$XYZ$, the moving coordinate system of the moving platform is set as $o$-$xyz$, and $\boldsymbol{r}_i$ $(i = 1, 2, \ldots, 8)$ is the length vector from point $p$ to $\boldsymbol{a}_i$; $\boldsymbol{A}_i$ is the outgoing point of the rope; $\boldsymbol{a}_i$ is the connection point between the rope and the strap. The coordinates of the cable outlet points of the thigh cable drive mechanism in the fixed coordinate system are ${}^O\boldsymbol{A}_i = \begin{bmatrix} X_{Ai} & Y_{Ai} & Z_{Ai} \end{bmatrix}^{\mathrm{T}}$ $(i = 1, 2, \ldots, 8)$; the coordinates of the connection point between the rope and the thigh strap in the moving platform coordinate system are ${}^p\boldsymbol{a}_i = \begin{bmatrix} x_{Ai} & x_{Ai} & x_{Ai} \end{bmatrix}^{\mathrm{T}}$ $(i = 1, 2, \ldots, 8)$, respectively.

The inverse kinematics analysis of robot is very important for the precise control and complex space operation tasks of robot. The inverse kinematics analysis of the robot, also known as the inverse solution, refers to the position and attitude of the given robot end effector in space, and solves the joint variables required to achieve this position and attitude [15–19]. The specific analysis process is as follows:

It is assumed that the moving coordinate system rotates $\alpha$, $\beta$ and $\gamma$ angles relative to the fixed coordinate system around the $X$, $Y$ and $Z$ axes of the fixed coordinate system, respectively. Therefore, the rotation matrix ${}^O\boldsymbol{R}_p$ from the fixed coordinate system to the moving coordinate system is

$$ {}^O\boldsymbol{R}_p = \boldsymbol{R}(Z,\gamma)\,\boldsymbol{R}(Y,\beta)\,\boldsymbol{R}(X,\alpha) = \begin{bmatrix} \boldsymbol{A_1} & \boldsymbol{A_2} & \boldsymbol{A_3} \end{bmatrix}. \tag{3} $$

Here:

$\boldsymbol{R}(Z,\gamma)$ – rotation matrix of $\gamma$-angle around $Z$-axis;

$$ \boldsymbol{R}(Z,\gamma) = \begin{bmatrix} \cos\gamma & -\sin\gamma & 0 \\ \sin\gamma & \cos\gamma & 0 \\ 0 & 0 & 1 \end{bmatrix}; $$

$\boldsymbol{R}(Y,\beta)$ – rotation matrix of $\beta$-angle around $Y$-axis;

$$\boldsymbol{R}(Y,\beta) = \begin{bmatrix} \cos\beta & 0 & \sin\beta \\ 0 & 1 & 0 \\ -\sin\beta & 0 & \cos\beta \end{bmatrix};$$

$\boldsymbol{R}(X,\alpha)$ – rotation matrix of $\alpha$-angle around $X$-axis;

$$\boldsymbol{R}(X,\alpha) = \begin{bmatrix} 1 & 0 & 0 \\ 0 & \cos\alpha & -\sin\alpha \\ 0 & \sin\alpha & \cos\alpha \end{bmatrix};$$

$$\boldsymbol{A}_1 = \begin{bmatrix} \cos\beta\cos\gamma \\ \cos\beta\sin\gamma \\ -\sin\beta \end{bmatrix}; \boldsymbol{A}_2 = \begin{bmatrix} \cos\gamma\sin\alpha\sin\beta - \cos\alpha\sin\gamma \\ \cos\alpha\cos\gamma + \sin\alpha\sin\beta\sin\gamma \\ \cos\beta\sin\alpha \end{bmatrix};$$

$$\boldsymbol{A}_3 = \begin{bmatrix} \cos\alpha\cos\gamma\sin\beta + \sin\alpha\sin\gamma \\ \cos\alpha\sin\beta\sin\gamma - \cos\gamma\sin\alpha \\ \cos\alpha\cos\beta \end{bmatrix}.$$

The inverse kinematics analysis of the rope traction skating training robot is to solve the rope length $l_i$ $(i = 1, 2, \ldots, 8)$ by giving the position ${}^{O}\boldsymbol{p}(x, y, z)$ and attitude angle $(\alpha, \beta, \gamma)$ of the moving coordinate system in the fixed coordinate system. The position vector of in the fixed coordinate system is expressed as follows

$$\overrightarrow{\boldsymbol{A}_i\boldsymbol{a}_i} = \overrightarrow{Op} + \overrightarrow{pa_i} - \overrightarrow{OA_i}\,. \tag{4}$$

Similarly, the vector relationship can be obtained as follows

$$\boldsymbol{L}_i = {}^{P}\boldsymbol{O} + {}^{O}\boldsymbol{R}_P {}^{P}\boldsymbol{a}_i - {}^{O}\boldsymbol{A}_i\,. \tag{5}$$

Therefore, the length of the $i$-th rope is:

$$\boldsymbol{l}_i = \|\boldsymbol{L}_i\| = \left\|\overrightarrow{A_i a_i}\right\|. \tag{6}$$

### 4.2. Forward kinematics analysis

After obtaining the inverse solution of the kinematic position, the forward calculation of the kinematic position of the mechanism is carried out, that is, the rotation angle of each joint of the lower limb is solved according to the known length change of each rope. This problem is a nonlinear multi-solution problem, which needs to be solved by numerical methods [20, 21]. The Levenberg-Marquardt algorithm is used to transform the forward kinematics problem into the least squares solution of the nonlinear overdetermined equations [22]. The Levenberg-Marquardt algorithm is a trust region method, which can adaptively switch between the Gauss-Newton method and the steepest descent method, thus taking into account the convergence speed and stability. Firstly, the objective function is constructed as follows:

$$F_i(x, l_i) = \|L_i\| - l_i\,, \qquad i = 1, 2, \ldots, m. \tag{7}$$

Here, $x$ is the parameter vector composed of joint angle, and $l_i$ is the independent variable composed of rope length. Let the objective function $F_i(x, l_i) = 0$ construct nonlinear equations. The residual vector $\boldsymbol{r}(x, l_i)$ of the equations is calculated, and a damping factor $\lambda$ is set to avoid the non-positive definite Hessian matrix of the nonlinear overdetermined equations. The search increment $h$ of the incremental equation $(\boldsymbol{H} + \lambda \boldsymbol{I})h = \boldsymbol{J}^{\mathrm{T}}\boldsymbol{r}$ is solved, where $\boldsymbol{H} = \boldsymbol{J}^{\mathrm{T}}\boldsymbol{J}$ is the Hessian matrix, and the Jacobian matrix $\boldsymbol{J}$ is expressed as follows:

$$\boldsymbol{J} = \nabla F_i(x, l_i) = \begin{bmatrix} \dfrac{\partial F_1(x, l_1)}{\partial x_1} & \dfrac{\partial F_1(x, l_1)}{\partial x_2} \\ \vdots & \vdots \\ \dfrac{\partial F_m(x, l_1)}{\partial x_1} & \dfrac{\partial F_m(x, l_1)}{\partial x_2} \end{bmatrix}. \tag{8}$$

The given initial sagittal and coronal rotation angles of the hip joint are taken as the initial iteration point $x_k$ coordinates, and then the function value $F_i(x_k, l_i)$ of the current point $x_k$ is calculated. After the search increment $h$ is obtained, the next iteration is carried out, and the new residual sum of squares $S(x_{k+1})$ is calculated. If $S(x_{k+1}) > S(x_k)$, the new iterative calculation results are accepted and the damping coefficient is reduced. Otherwise, the results are rejected and the damping coefficient is increased. In order to avoid the divergence of the iterative results, the input independent variable $l_i$ should be selected from the inverse solution results of the kinematic position, and two sets of parameters should be selected for verification. The results are shown in Table 3 and Table 4. From Table 4, it can be seen that the error of hip joint rotation angle is kept after three decimal points,

Table 3. Kinematics position inverse solution results

| Parameters | First group | Second group |
|---|---|---|
| $\alpha$ [°] | 0.2095 | –9.6784 |
| $\beta$ [°] | 0.9037 | 3.1806 |
| $l_1$ [m] | 1.1601 | 1.1192 |
| $l_2$ [m] | 8.4563 | 0.8295 |
| $l_3$ [m] | 1.0951 | 0.9984 |
| $l_4$ [m] | 1.1584 | 1.1975 |
| $l_5$ [m] | 0.8447 | 0.8728 |
| $l_6$ [m] | 1.0591 | 1.1496 |
| $l_7$ [m] | 1.0487 | 1.0262 |
| $l_8$ [m] | 1.1245 | 1.1153 |

Table 4. Forward solution results of kinematic position

| Parameters | First group | Second group |
|---|---|---|
| $l_1$ [m] | 1.1602 | 1.1191 |
| $l_2$ [m] | 8.4562 | 0.8294 |
| $l_3$ [m] | 1.0957 | 0.9985 |
| $l_4$ [m] | 1.1581 | 1.1974 |
| $l_5$ [m] | 0.8445 | 0.8724 |
| $l_6$ [m] | 1.0591 | 1.1497 |
| $l_7$ [m] | 1.0486 | 1.0261 |
| $l_8$ [m] | 1.1244 | 1.0263 |
| $\alpha$ [°] | 0.2087 | –9.6736 |
| $\beta$ [°] | 0.9014 | 3.1803 |

which proves the correctness and accuracy of forward kinematics algorithm and inverse kinematics analysis.

## 4.3. Workspace analysis

### 4.3.1. Static analysis

Compared with the traditional rigid mechanism, the rope traction skating training robot is flexible. Compared with the rod, the rope is flexible, can only apply one-way tension, cannot bear the pressure. Therefore, the rope-driven skating training robot must have force redundancy, that is, meet the force vector closure principle [23]. Now, the static analysis is carried out. $\boldsymbol{L}_i$ is the cable vector from $\boldsymbol{A}_i$ to $\boldsymbol{a}_i$, $\boldsymbol{u}_i = \boldsymbol{L}_i/l_i$ is the unit vector of the cable, $\boldsymbol{u}_i = \boldsymbol{L}_i/l_i$ is the tension of the $i$-th cable, $\boldsymbol{f}_p$ and $\boldsymbol{t}_p$ are the other resultant forces and moments acting on the thigh cable driving mechanism except the cable tension.

According to the principle of static balance, the force spiral balance equation of the thigh rope driving mechanism is

$$\sum_{i=1}^{8} \boldsymbol{f}_i + \boldsymbol{f}_p = 0, \tag{9}$$

$$\sum_{i=1}^{8} \boldsymbol{r}_i \times \boldsymbol{f}_i + \boldsymbol{t}_p = 0. \tag{10}$$

Derived from (10)

$$\boldsymbol{J}^{\mathrm{T}}\boldsymbol{T} = \begin{bmatrix} \boldsymbol{u}_1 & \boldsymbol{u}_2 & \cdots & \boldsymbol{u}_8 \\ \boldsymbol{r}_1 \times \boldsymbol{u}_1 & \boldsymbol{r}_2 \times \boldsymbol{u}_2 & \cdots & \boldsymbol{r}_8 \times \boldsymbol{u}_8 \end{bmatrix} \boldsymbol{T}. \tag{11}$$

Here:

$\boldsymbol{J}$ – the force Jacobian matrix;

$\boldsymbol{T}$ – the tension matrix of the rope; $\boldsymbol{T} = \begin{bmatrix} f_1 & f_2 & \cdots & f_8 \end{bmatrix}^{\mathrm{T}}$;

$\boldsymbol{r}_i$ – the length vector from $p$ to $\boldsymbol{a}_i$.

### 4.3.2. Controllable workspace

In the $n$-degree-of-freedom robot mechanism driven by $m$ ropes, when $\mathrm{rank}(\boldsymbol{J}^{\mathrm{T}}) = n$, any set of $n$ vectors in the direction vector of $m$ ropes is linearly independent, so it satisfies the vector closure principle [24]. Verhoeven [25] derived a necessary and sufficient condition for the pose of the moving platform in the controllable workspace, namely null space $N(\boldsymbol{J}^{\mathrm{T}}) > 0$. The controllable workspace of the rope drive mechanism is the working area of the moving platform, which determines the movable range of the moving platform and is an important index to measure the performance of the mechanism [26].

According to the solution process of the workspace shown in Fig. 9, this paper uses the Monte Carlo method to solve the cable drive mechanism in the MATLAB

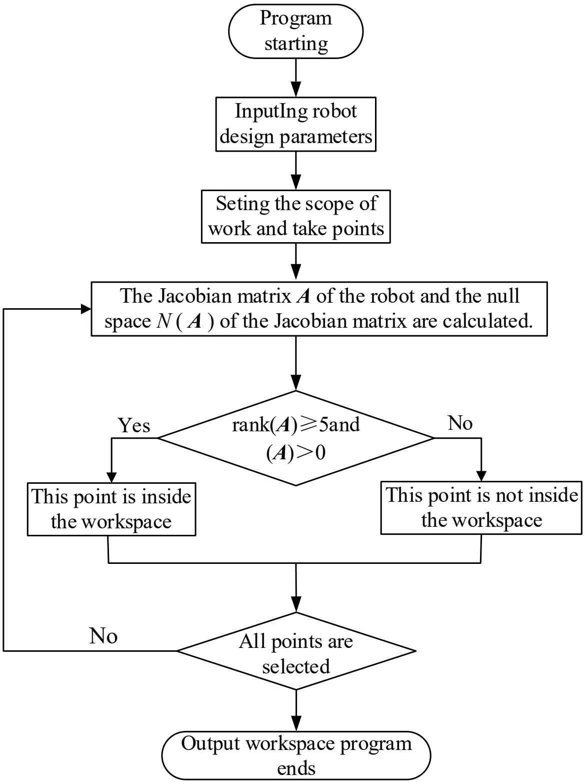

Fig. 9. Solving process of controllable workspace of skating training robot

environment. In the set working range, 10000 points are randomly selected, and the corresponding pose of each point is obtained, so as to obtain the controllable working space of the cable driving mechanism at different pose angles.

Fig. 10 is a three-dimensional diagram of the controllable workspace when the thigh rope driving mechanism rotates around the hip joint. Figs. 11, 12 and 13 are the projections of the three-dimensional controllable workspace along the *XOZ*, *XOY* and *YOZ* planes, respectively. The shadow area in Fig. 10 is the controllable working range of the mechanism. The following conclusions can be clearly drawn from Figs. 10–13.

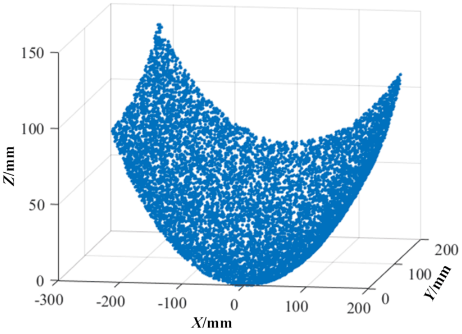

Fig. 10. Controllable workspace of thigh rope driving mechanism

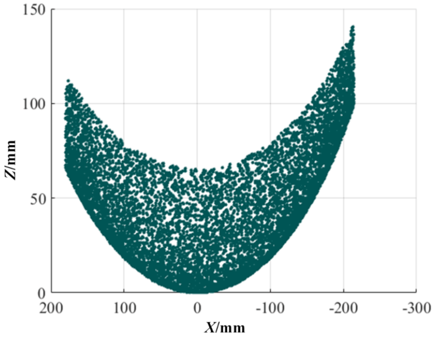

Fig. 11. XOZ projection of three-dimensional controllable workspace

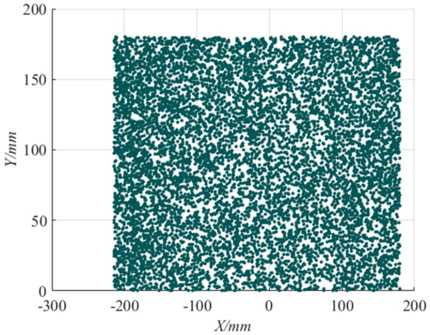

Fig. 12. XOY projection of three-dimensional controllable workspace

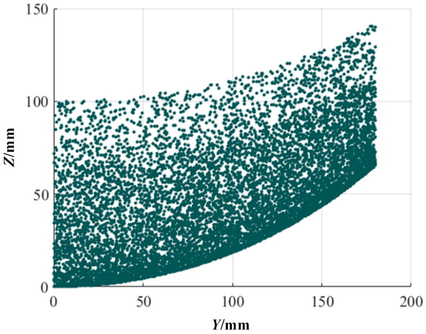

Fig. 13. YOZ projection of three-dimensional controllable workspace

1. Through the three-dimensional diagram of the controllable workspace when the thigh rope driving mechanism rotates around the hip joint, it can be seen that the three-dimensional diagram shows an arc-like rising state, which is due to the joint rotation of the hip joint around the sagittal plane and the coronal plane.

2. Through the three-dimensional image of the controllable working space when the thigh rope drive mechanism rotates around the hip joint, it can be seen

that the height of the $Z$ direction decreases first and then increases within the specified rotation angle range along the sagittal plane, and reaches the lowest point when the rotation angle is 0; the height of the $Z$ direction increases first and reaches the lowest point when the rotation angle is 0 within the specified rotation angle range along the coronal plane.

3. Through the top view of the three-dimensional image of the controllable workspace when the thigh rope drive mechanism rotates around the hip joint, it can be seen that there are no singular points in the workspace, indicating that the structure has good reliability.

### 4.3.3. Controllable workspace

In order to verify the correctness of the above conclusions, the control variable method was used to set the hip joint to rotate 0°, 10°, 20°, 30° along the coronal plane and the hip joint to rotate −50°, −40°, −30°, −20°, −10°, 0°, 10°, 20°, 30°, 40° along the sagittal plane, and observe its controllable working space. Fig. 14 shows the relationship between the controllable workspace and the rotation of the hip joint along the sagittal plane.

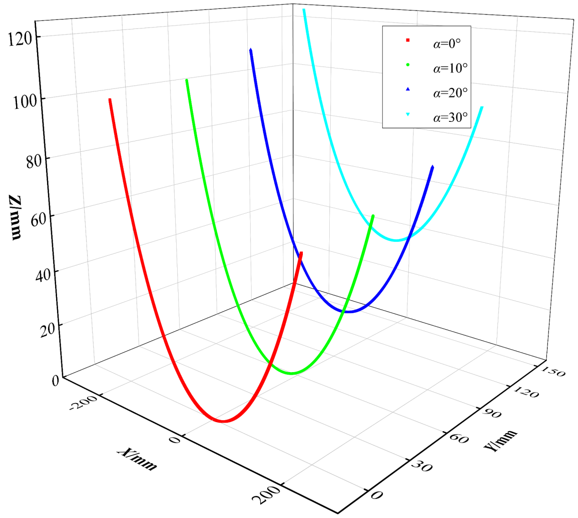

Fig. 14. The relationship between controllable workspace and hip joint rotation along the sagittal plane relationship

Fig. 15 shows the relationship between the controllable workspace and the rotation of the hip joint along the coronal plane.

Through the analysis of Figs. 14–15, it can be seen that the conclusions obtained in Section 4.3.2 are reasonable.

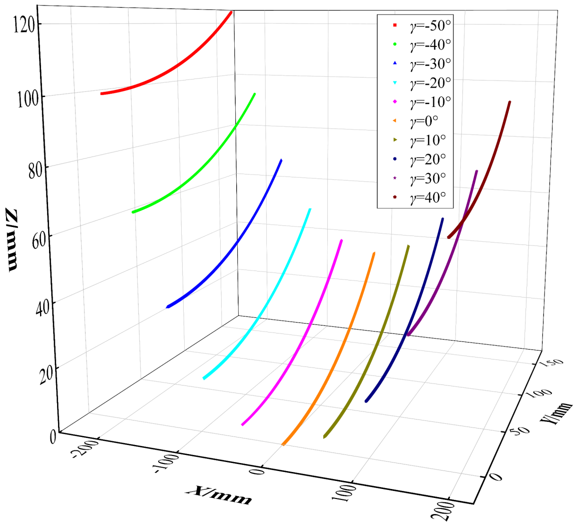

Fig. 15. The relationship between controllable workspace and hip joint rotation along the coronal plane

#### 4.3.4. Actual workspace

In the Matlab environment, under the premise that the hip joint is known to be active along the coronal and sagittal angles of $-50^\circ \div 40^\circ$ and $0^\circ \div 30^\circ$, the trajectory of the geometric center point of the driving mechanism of the skating training robot can be obtained. The actual working space reached by the athletes in the skating training process is shown in Fig. 16, which shows the actual working space of the skating training robot.

The actual workspace of the rope-driven skating training robot is solved based on the overall structure and the range of activities achieved by the overall training process, while the controllable workspace is solved by using structural segmen-

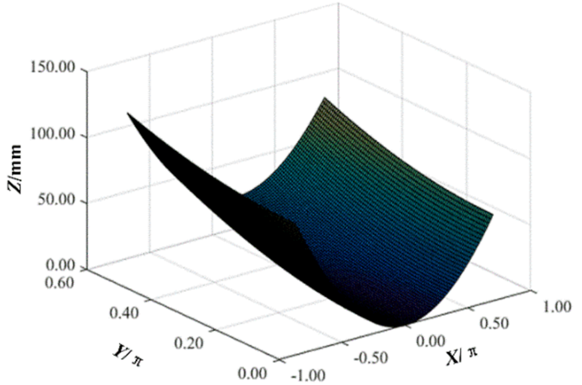

Fig. 16. The actual working space of the skating training robot

tation and control variables within the controllable range of different angles of the driving mechanism. By comparing the actual working space range with the minimum controllable working space range, it can be seen that the actual working space has been within the controllable working space range, which shows that the configuration scheme of the skating training robot can meet the needs of the actual training of the athletes, and proves the rationality of the mechanism configuration.

## 5. Real-time forward kinematics algorithm

After completing the inverse kinematics analysis, forward kinematics position verification and workspace analysis of the rope-driven skating training robot, a forward kinematics real-time algorithm is proposed. The algorithm combines interval analysis with Levenberg-Marquardt iterative solver. Compared with the traditional numerical solution forward kinematics algorithm, it shortens the iterative calculation time on the basis of ensuring its original ability to analyze the singularity of the structure, and can be used for real-time control of the rope-driven skating training robot. When solving the forward kinematics, the numerical iteration method alone may cause the results to be unable to converge. However, the interval analysis alone can improve the calculation accuracy, but the calculation time is too long to ensure the real-time performance of the algorithm. Therefore, the two methods are combined. Firstly, the initial solution of the pose of the end moving platform is estimated by interval analysis and the boundary range of the result is guaranteed. Secondly, the Levenberg-Marquardt algorithm is used to iterate the platform pose according to the initial estimation value through the least square method of nonlinear equations.

### 5.1. Algorithm introduction

The first step of the algorithm is to determine the initial estimate of attitude $P_0$. In order to estimate the initial position of the platform, a method inspired by interval analysis is adopted. The core goal is to strictly limit the position of the tool center point TCP of the end-moving platform by placing the axis-aligned bounding box around the outgoing point. For the rope-driven ski training robot, the out-of-rope point $A_i$ is distributed around the workspace of the end moving platform. Therefore, the intersection area of these bounding boxes is relatively small and can be used as an initial estimate of the location.

Fig. 17 is a simplified rope-moving platform vector closed model, where vector $\boldsymbol{a}_i$ represents the position of the near-end rope point $\boldsymbol{A}_i$ on the frame, vector $\boldsymbol{b}_i$ represents the relative position of the far-end traction point $P_i$ on the end moving platform, and $\boldsymbol{L}_i$ represents the vector of the rope. Let's establish a vector closed equation as shown below:

$$\boldsymbol{a}_i - \boldsymbol{r} - \boldsymbol{R}\boldsymbol{b}_i - \boldsymbol{L}_i = 0, \qquad i = 1, 2, \ldots, m. \tag{12}$$

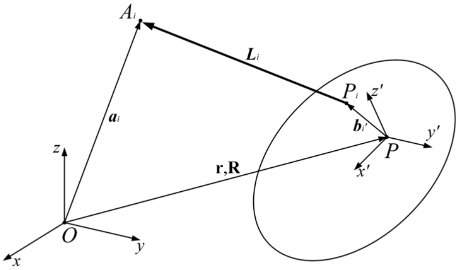

Fig. 17. Vector closed model of rope-moving platform

Here, vector $\boldsymbol{r}(x, y, z)$ is the position of the platform, rotation matrix $\boldsymbol{R}(\alpha, \beta)$ represents the direction of the platform, and $m$ represents the number of ropes.

Firstly, the closed vector expression of the rope-moving platform model is rewritten as

$$\boldsymbol{a}_i - \boldsymbol{r} = \boldsymbol{l}_i + \boldsymbol{R}\boldsymbol{b}_i\,. \tag{13}$$

Since the rotation matrix is orthogonal in structure, the rotation matrix $\boldsymbol{R}$ is deleted by using the triangle inequality, and the rotation matrix $\boldsymbol{R}$ is obtained.

$$\|\boldsymbol{R}\boldsymbol{b}_i\|_2 = \|\boldsymbol{b}_i\|_2\,. \tag{14}$$

Therefore, the equation (12) can be expressed by the triangle inequality as follows

$$\|\boldsymbol{a}_i - \boldsymbol{r}\|_2 \leqslant \boldsymbol{l}_i + \|\boldsymbol{b}_i\|_2\,. \tag{15}$$

It can be concluded from equation (15) that the TCP of the end moving platform is located in a sphere with a radius around the rope point. By enclosing the sphere with a box and estimating its interval, the following boundary can be obtained.

$$\begin{aligned} \boldsymbol{r}_i^{\text{low}} &= \boldsymbol{a}_i - \left(l_i + \|b_i\|_2\right)\left[1, 1\right], \\ \boldsymbol{r}_i^{\text{high}} &= \boldsymbol{a}_i - \left(l_i + \|b_i\|_2\right)\left[1, 1\right]. \end{aligned} \tag{16}$$

Then, the intersection of all $m$ bounding boxes is calculated, namely

$$\boldsymbol{r}^{\text{low}} = \max_i \boldsymbol{r}_i^{\text{low}}, \tag{17}$$

$$\boldsymbol{r}^{\text{high}} = \max_i \boldsymbol{r}_i^{\text{high}}. \tag{18}$$

Let's select the center $\boldsymbol{r}_o = (\boldsymbol{r}^{\text{low}} + \boldsymbol{r}^{\text{high}})/2$ of the bounding box range as the initial estimate. If $\boldsymbol{r}^{\text{low}} > \boldsymbol{r}^{\text{high}}$, it is proved that the end pose has no solution at this time.

Fig. 18. is a simplified example of the planar rope moving platform of the thigh segment. The dotted circle is centered on the rope point $A_i$, and the radius is $l_i + \|\boldsymbol{b}_i\|_2$. The solid line bounding box represents the interval estimates of

these circles. The light gray rectangle is the cross area of the bounding box of 8 ropes, which is included in TCP. The dark gray area can usually give a better estimate by calculating the intersection of the dotted circles. However, due to the addition of more bounding box boundary constraints, the calculation process is more complicated. Therefore, the Levenberg-Marquardt iterative solver is started at the center point of the light gray box.

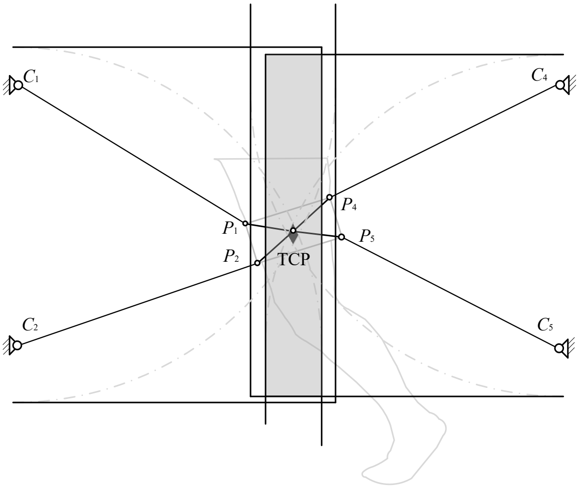

Fig. 18. Axis-aligned bounding box model

In order to determine the pose $p$ of the moving platform of the rope-driven skating training robot, the Levenberg-Marquardt iterative solver is used. Given a function $\boldsymbol{\psi}$: $R^n \rightarrow R^m$ : and $\|\boldsymbol{\psi}(p)\|_2$, the Levenberg-Marquardt algorithm can be used to obtain the pose parameter $p$ that is minimized. The algorithm is implemented by the iterative process $p_{i+1} = p_i + h$, in which the step $h$ of the Levenberg-Marquardt algorithm is determined by the linear system equation (19).

$$\left[\boldsymbol{J}(p_i)\boldsymbol{J}^{\mathrm{T}} + \mu\boldsymbol{I}\right]\boldsymbol{h} = \boldsymbol{J}^{\mathrm{T}}(p_i)\boldsymbol{\psi}(p), \tag{19}$$

where $\mu$ is the damping parameter and $\boldsymbol{J}(p_i)$ is the Jacobian matrix of $\boldsymbol{\psi}(p_i)$.

If the iteration change under the current step is very small, that is, $\|h_i\|_2 < \varepsilon_2(\|p_i\|_2 + \varepsilon_2)$, or $\|\boldsymbol{J}^{\mathrm{T}}(p_i)\boldsymbol{\psi}(p_i) < \varepsilon_1\|$, the program terminates and the thresholds are set manually.

### 5.2. Convergence effect and real-time evaluation of real-time kinematics algorithm

It is needed to verify the convergence effect of the real-time kinematics algorithm and evaluate its real-time performance. According to the workspace analysis of Section 4.3, the rotation angle $\alpha$ of the moving platform around the $x$-axis is selected as 0 and the human thigh is verified and evaluated when moving in the sagittal plane.

According to equation (12), $m$ nonlinear equations of forward kinematics are obtained, and a set of nonlinear overdetermined equations is formed, as shown in equation (20).

$$\boldsymbol{\psi}_i(\boldsymbol{l},\boldsymbol{r},\boldsymbol{R}) = \|\boldsymbol{a}_i - \boldsymbol{r} - \boldsymbol{R}\boldsymbol{b}_i\|_2 - l_i^2 , \qquad i = 1, 2, \ldots, m. \tag{20}$$

The nonlinear overdetermined equations cannot be solved accurately, so the problem of solving the equations is transformed into an optimization problem, that is, using the least square method, the equations are expressed in the form of residual sum of squares as shown in equation (21).

$$\phi(l) = \min_{r,R} \sum_{i}^{m} \boldsymbol{\psi}_i(\boldsymbol{l},\boldsymbol{r},\boldsymbol{R}). \tag{21}$$

Among them, $\boldsymbol{l} = [l_1, \ldots, l_m]^{\mathrm{T}}$ is the vector composed of rope length. The optimization function $\phi(\boldsymbol{l})$ can get the minimum $r^*$ and $R^*$ values on the right side of the equal sign. The vector coordinate transformation of equation (22) is carried out, and the rotation matrix $\boldsymbol{R}$ and vector $\boldsymbol{r}$ are parameterized as follows:

$$\phi(l, x, z, \beta) = \sum^{m} \left(A^2 + B^2 + l_i^2\right)^2 . \tag{22}$$

Here $A = -\sin(\beta)x_{pi} - \cos(\beta)z_{pi}$; $B = \cos(\beta)x_{pi} - \sin(\beta)z_{pi}$.

The gradient $G$ includes three partial derivatives of the objective function, and because the objective function is $\phi(l, x, z, \beta)$ differentiable, the optimal estimate searched by the iterative solver should be the pose of $\phi(l, x, z, \beta) = 0$ when the exact rope length is given in the forward kinematics calculation. In addition, after obtaining the gradient of the objective function, it is also necessary to consider solving its Hessian matrix to characterize the number and type of extreme values of the objective function. The representation of the Hessian matrix is:

$$\boldsymbol{H}_v = \begin{bmatrix} \dfrac{\partial^2\phi}{\partial x \partial x} & \dfrac{\partial^2\phi}{\partial x \partial z} & \dfrac{\partial^2\phi}{\partial x \partial \beta} \\ \dfrac{\partial^2\phi}{\partial x \partial z} & \dfrac{\partial^2\phi}{\partial z \partial z} & \dfrac{\partial^2\phi}{\partial z \partial \beta} \\ \dfrac{\partial^2\phi}{\partial x \partial \beta} & \dfrac{\partial^2\phi}{\partial z \partial \beta} & \dfrac{\partial^2\phi}{\partial \beta \partial \beta} \end{bmatrix} . \tag{23}$$

The sufficient condition for the unique optimal value of the function $\phi$ is that the gradient $\boldsymbol{G} = 0$ and the Hessian matrix $\boldsymbol{H}_v$ is a positive definite matrix. According to the Schwarz theorem [27], the Hessian matrix $\boldsymbol{H}_v$ is a symmetric matrix because the objective function $\phi$ is continuously derivable in the pose $P(x, z, \beta)$. Therefore, whether the matrix is a positive definite matrix can be verified by testing whether the determinant is positive. If the determinant is positive, both eigenvalues are positive.

The rope arrangement scheme and the geometric parameters of the end moving platform of each segment of the lower limb are substituted into the determinant of the Hessian matrix $\boldsymbol{H}_v$, and the determinant becomes a multivariate polynomial composed of the pose $P(x, z, \beta)$ and the rope length $\boldsymbol{l} = [l_1, \ldots, l_m]^{\mathrm{T}}$. In order to eliminate the dependence of the matrix determinant on the rope length, the inverse kinematics position equation in (19) is substituted into the matrix, ignoring the influence of the rope length noise on the result.

Fig. 19 shows the variation of the determinant of the objective function Hessian matrix with the pose parameters $x$ and $z$ of the moving platform when the moving platform $\beta = -15°$, $\beta = 0°$, $\beta = 10°$, and $\beta = 20°$ are at the end of the thigh segment. The variation ranges of $x$ and $z$ are 0–1.6 m and 0–2 m, respectively. It can be seen from the above figure that the calculation results of the Hessian matrix determinant in the four cases are all positive, that is, the Hessian matrix is a positive definite matrix, indicating that in the given workspace of the end moving platform, the local minimum of the corresponding constraint objective function can be found in any pose, and the best estimate of the pose can be obtained.

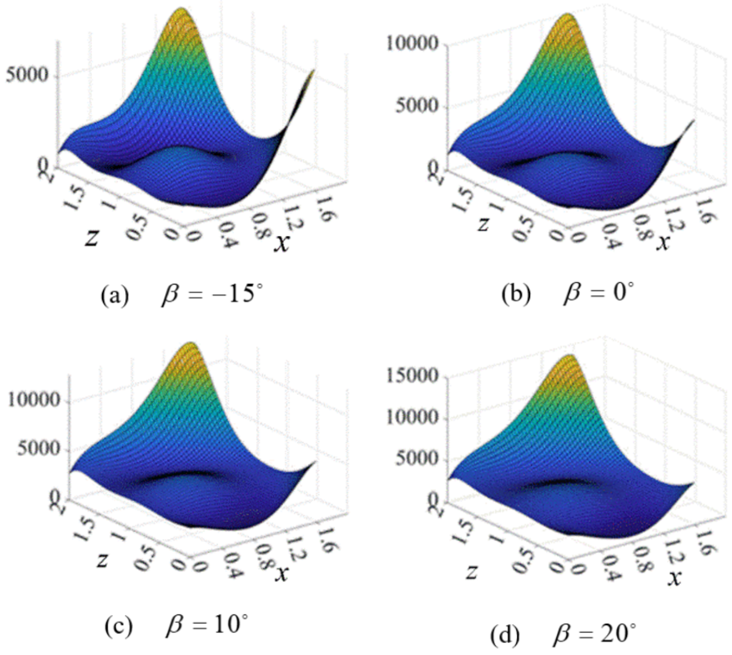

(a) $\beta = -15^{\circ}$ (b) $\beta = 0^{\circ}$

(c) $\beta = 10^{\circ}$ (d) $\beta = 20^{\circ}$

Fig. 19. Evaluates the determinant calculation results of the objective function Hessian matrix

In the workspace of the end moving platform obtained by the optical motion capture experiment, 500 pose $P_i$ are randomly selected, and three different amplitudes of noise of 0.1 mm, 0.5 mm and 1 mm are added to the rope length input in the forward kinematics real-time algorithm to simulate the measurement and control error. The two thresholds $\varepsilon_1$ and $\varepsilon_2$ in the iteration termination condition of the Levenberg-Marquardt iterative solver are set to $10^{-17}$, the initial damping parameter $\mu$ is set to $10^{-3}$, and the maximum number of iterations is set to 50.

Since the Windows operating system lacks a high-precision timer with a resolution of less than 1 ms, it is impossible to accurately obtain the single iteration calculation time. Therefore, the average of 500 iteration times is taken as the standard to measure the real-time performance of the algorithm. In addition, the distribution of the number of iterations required for convergence is collected and represented in Fig. 20. Fig. 20a to 20c are the histograms of the number of iterations of applying 0.1, 0.5, and 1 mm noise to the length of the rope, respectively. Fig. 20d

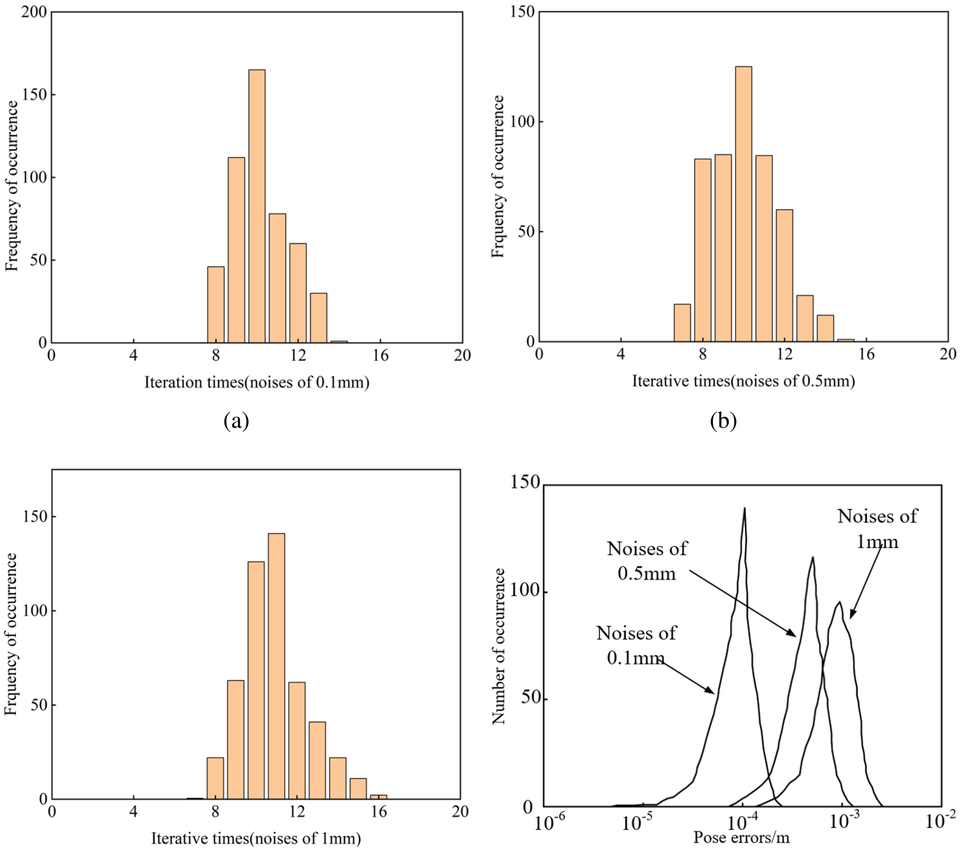

(a) (b)

(c) (d)

Fig. 20. Numerical results of forward kinematics calculation based on Levenberg-Marquardt algorithm

shows the pose error histograms of 0.1 mm, 0.5 mm and 1 mm noise applied to the rope length, respectively. From Fig. 20a, 20b and 20c, it can be concluded that for all poses in a given workspace, the number of iterations of the algorithm is between 7 and 20, and it usually requires 10 iterations, with an average iteration time of 46 ms. Fig. 20d shows that the error between the expected pose and the calculated pose is related to the noise in the rope length, and the average error of the pose is almost equal to the noise of the rope length.

## 6. Gait planning control experiment

In order to realize the normal skating gait in the sagittal and coronal planes of the rope-driven lower limb robot, the robot control system is designed, and the experimental platform is built to carry out the gait planning control experiment. The control program is written by Visual Studio software, and the pose of the end moving platform is controlled by changing the rope length of the eight traction ropes of the unilateral lower limb. Siemens S7-1200 PLC is used as the server of PC client, and the communication mode is connected by Snap7 software package based on S7 protocol. The robot control signal path is shown in Fig. 21.

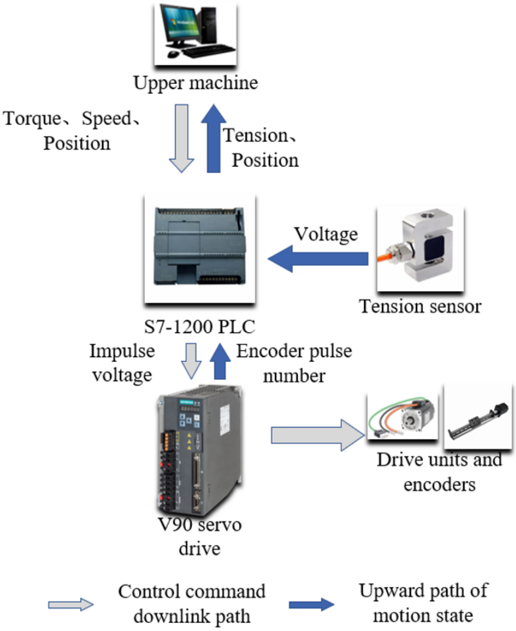

Fig. 21. Axis-aligned bounding box model

The gait planning control experiment of skating training is designed, and the PID position closed-loop of the end moving platform is established to obtain the pose information of the end moving platform. The pose information is compared with the theoretical derivation expectation to verify the correctness of the kinematics theoretical derivation and gait planning simulation. Through the Snap7 library, the communication and control instructions are sent between the PC host computer and the S7-1200 PLC, and the real-time control of the terminal moving platform of the skating training robot is realized.

According to the gait of human skating, the expected motion trajectory of the end moving platform of the subject is calculated, and a motion period is set to 10 s. The trajectory is discretized according to time, and the sampling period is 10 ms. In the experiment, the slider of the ball screw is first positioned by the photoelectric position switch on the slide rail. At this time, the tension sensor value on the rope is read to ensure that the rope meets the preload requirements. The upper computer transmits the variation to the S7-1200 PLC. The PLC zooms and standardizes the control signal through the PROFINET communication interface, so that the analog quantity is sent to the torque command input port of the V90 servo driver. The servo driver completes the position control closed-loop of the motor, so that the slider can pull the rope to pull the end moving platform according to the motion trajectory under the gait planning. The walking situation in a skiing gait cycle is shown in Fig. 22.

Fig. 22. Walking situation in a skating gait cycle

The real-time forward kinematics algorithm is used to calculate the average value of the rope position information collected by the encoder in 50 gait cycles, and the pose of the end moving platform of the thigh segments corresponding to the acquisition point is obtained. The sampling value of the rope position and the calculation results of the real-time forward kinematics algorithm are compared and analyzed with the expected rope position change and the pose change of the end moving platform.

Fig. 23 shows the comparison between the average value and the expected value of the rope position variation collected by the encoder on some servo motors in one gait cycle.

The dotted line in the figure is the actual change of the rope position obtained by averaging the driving motor encoder in multiple cycles, and the solid

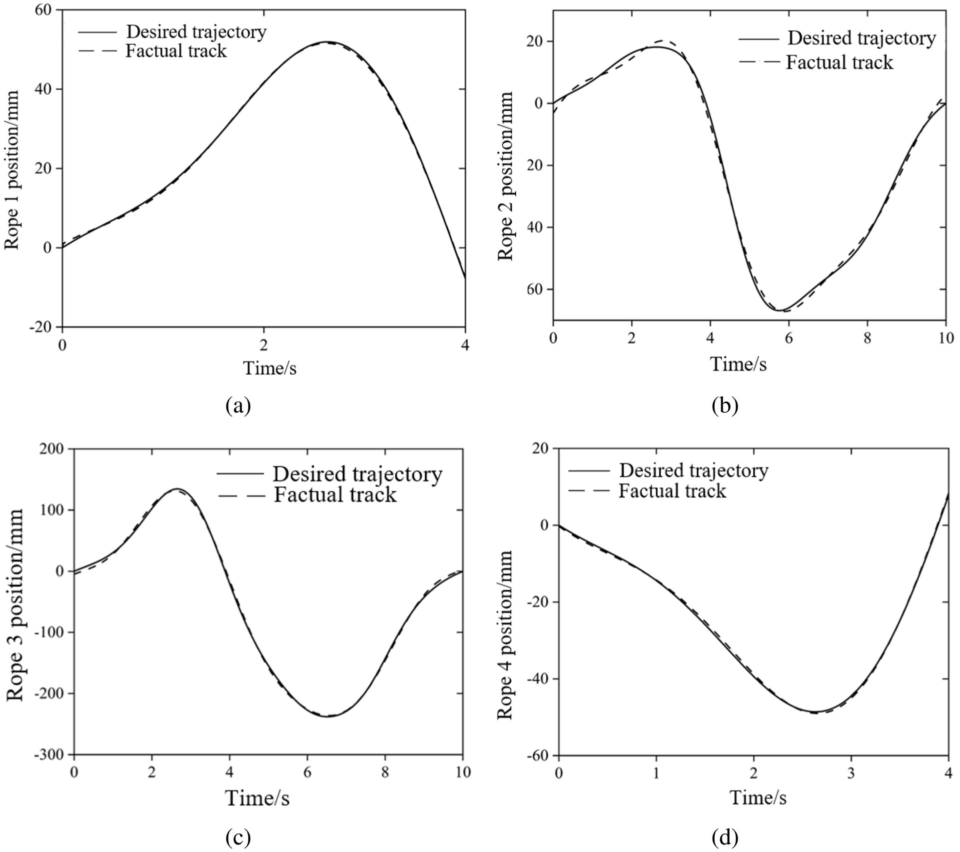

(a) (b)

(c) (d)

Fig. 23. Position variation of ball screw slider

line is the expected rope trajectory. Fig. 23b and Fig. 23c have obvious errors in the whole cycle compared with the other charts, so the whole cycle is taken as the horizontal axis range. From the experimental results, it can be seen that the actual rope length change trend of the rope-driven skating training robot is basically consistent with the expected trajectory, and the error is kept within 5mm. However, due to the elastic deformation of the rope and the end moving platform, the installation accuracy of the rope guiding module, the moment of inertia of the motor and the delay of the PLC response, there is still a certain deviation and lag between the end moving platform pose calculated by the real-time forward kinematics algorithm and the expected pose, as shown in Fig. 24. It can be seen from the figure that the displacement of the moving platform along the $x$ direction, $y$ direction and $z$ direction and the rotation angle tracking of the sagittal plane and coronal plane are good. The movement error is controlled within 6 mm, the rotation error is controlled at about 3°, and the lag time is about 0.23 s. The end-effector moving platform has a good tracking effect on the desired trajectory, and the experimental results are in line with expectations. The kinematics theoretical analysis is verified, and it is proved that the prototype platform can achieve the desired skating training trajectory under the specified walking speed.

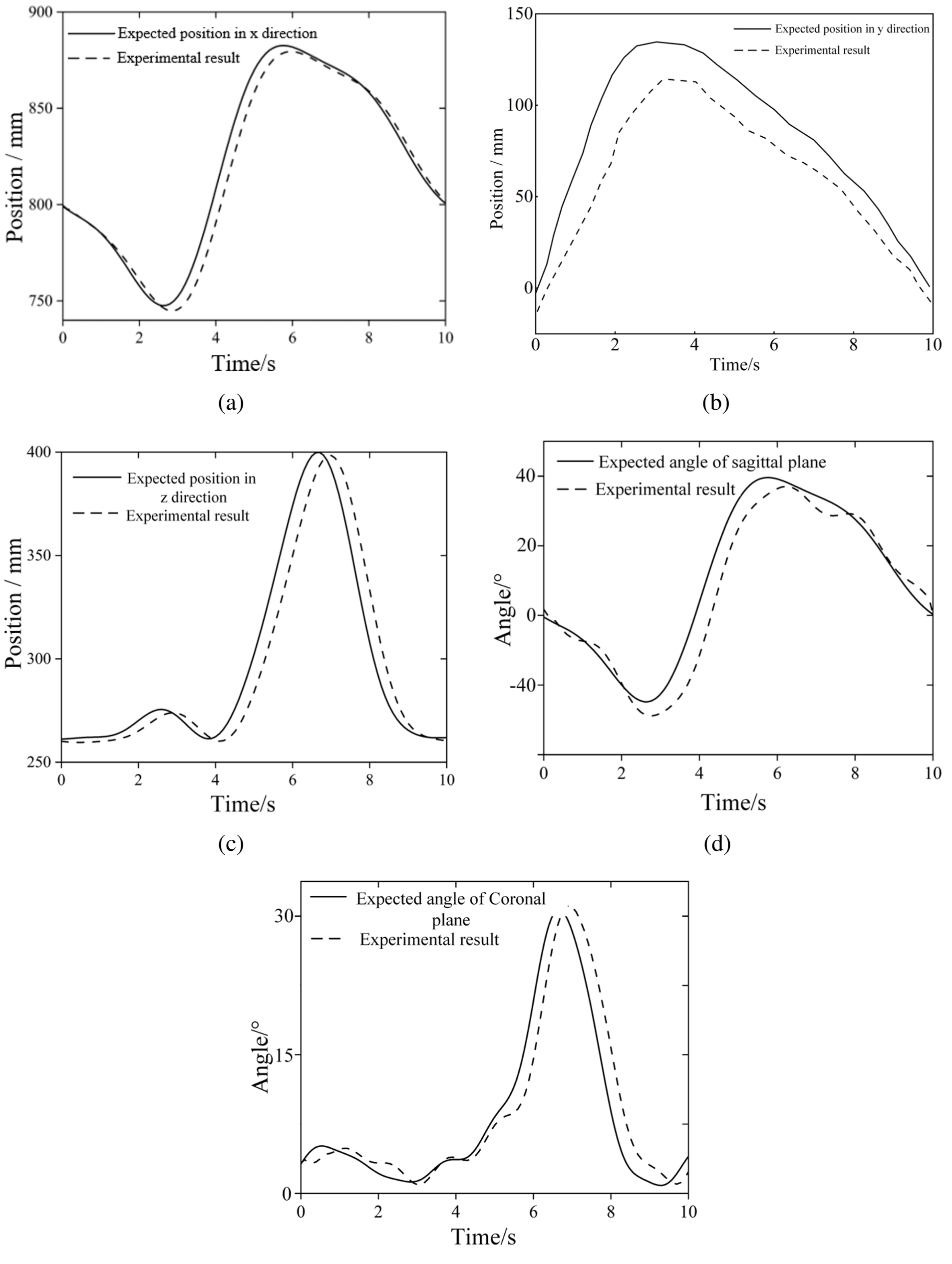

(a) (b)

(c) (d)

(e)

Fig. 24. Position variation of ball screw slider

## 7. Conclusion

Based on the rope parallel mechanism, a new type of rope-driven skating training robot configuration is proposed. The geometric model of the rope-driven skating training robot is established. The degree of freedom of the mechanism is analyzed. The forward kinematics of the robot is derived by Levenberg-Marquardt method. The controllable workspace and actual workspace of the robot are analyzed, and the workspace is solved. The results show that the actual workspace of the robot is within the controllable workspace. Based on interval analysis and Levenberg-Marquardt iterative solver, a real-time forward kinematics position algorithm is proposed, and the real-time performance and convergence ability of the real-time forward kinematics algorithm are verified. Finally, the prototype experimental platform is built and the gait planning control experiment is carried out. The experimental results show that the displacement of the moving platform in the $x$ direction, $y$ direction and $z$ direction and the rotation angle tracking effect of the sagittal plane and coronal plane are good. The movement error is controlled within 6 mm, the rotation error is controlled at about $3^\circ$, and the lag time is about 0.23 s. The correctness of the kinematics analysis and the feasibility of the mechanism are proved, which lays a foundation for the further optimization of the control system.

## References

[1] P. Liu and J. Zeng. Research on the development path of ice and snow sports entering campus under the background of the Beijing Winter Olympics Games. *International Journal of New Developments in Education*, 5(25):5–10, 2023. doi: 10.25236/IJNDE.2023.052502.

[2] Z. Chen. Research on the challenges and countermeasures of reserve talent cultivation in ice and snow sports. *Industry and Technology Forum*, 23(09):106–108, 2024.

[3] T. Wang, Z. Wu, J. Yu, M. Tan, and F. Zhang. Progress and perspective of ice and snow sport biomechanics and related robots. *Acta Automatica Sinica*, 45(09):1620–1636, 2019. doi: 10.16383/j.aas.c180720. (in Chinese).

[4] Chen Li. *The Biomechanical Simulation of Skiing Movement*. Ph.D. Thesis, Dalian University of Technology, China, 2009. (in Chinese).

[5] J. Sporri, J. Kroll, M. Gilgien, and E. Muller. How to prevent injuries in alpine ski racing: what do we know and where do we go from here? *Sports Medicine*, 47(4):599–614, 2017. doi: 10.1007/s40279-016-0601-2.

[6] C.A. Stuart. *Snow sport head injury: characterization of clinical presentation and design of a relevant head impact apparatus*. MASc Thesis, University of British Columbia, Canada, 2017. doi: 10.14288/1.0345635.

[7] M. Moncalero, S. Signetti, B. Mazzanti, P. Bruzzi, N.M. Pugno, and M. Colonna. Effect of material elastic properties and surface roughness on grip performances of ski boot soles under wet and icy conditions. *International Journal of Industrial Ergonomics*, 61:62–70, 2017. doi: 10.1016/j.ergon.2017.04.004.

[8] M. Colonna, M. Nicotra, and M. Moncalero. Materials, designs and standards used in ski-boots for alpine skiing. *Sports*, 1(4):78–113, 2013. doi: 10.3390/sports1040078.

[9] X. Fang. Maibu Robot: Accelerating the layout of the rehabilitation industry and helping patients walk again. *Robotics Industry*, 2021(02):66–71, 2021. doi: 10.3969/j.issn.2096-0182.2021.02.012. (in Chinese).

[10] D. Pisla, I. Nades, P. Tucan, S. Albert, G. Carbone, T. Antal, A. Banica, and B. Gherman. Development of a control system and functional validation of a parallel robot for lower limb rehabilitation. *Actuators*, 10(10):277–277, 2021. doi: 10.3390/act10100277.

[11] V. Mattoni E. Ida, and M. Carricato. Design of a planar cable-driven parallel robot for non-contact tasks. *Applied Sciences*, 11(20):9491–9491, 2021. doi: 10.3390/app11209491.

[12] J. Albus, R. Bostelman, and N. Dagalakis. The NIST RoboCrane. *Journal of Robotic Systems*, 10(5):709–724, 1993. doi: 10.1002/rob.4620100509.

[13] Wang Yiming, Wei Yishan, Hu Xiufang, et al. Design and optimization of lower limb rehabilitation robot driven by parallel ropes. *Journal of Biomedical Engineering Research*, 40(04):401–406, 2021.doi: 10.19529/j.cnki.1672-6278.2021.04.10. (in Chinese).

[14] Spidercam. [EB/OL] (2022-04-05) [2022-04-05]. `http://www.spidercam.org`.

[15] H.J. San, Y.M. Wang, and J.X. Liu. Analyzing moving character of a novel parallel mechanism. *Advanced Materials Research*, 605-607:1568–1572, 2013. doi: 10.4028/www.scientific.net/AMR.605-607.1568.

[16] Z. Meng, Z. Hao, Z. Sun and C. Ming. Kinematics analysis and optimization of the lower hook mechanism in netting machine. *Journal of Mechanical Science and Technology*, 38(5):2563–2577, 2024. doi: 10.1007/s12206-024-0435-z.

[17] L. Wu, X. Liu, M. Wang et al. Kinematic analysis of a spatial cable-driven mechanism and its equivalent hybrid mechanism for elliptical trajectory. *Machines*, 11(7):710, 2023. doi: 10.1007/s12206-024-0435-z.

[18] B. Hu, Z. Liu, J. Zhao, J. Zhao, and J. Yao. Kinematics analysis of 6-degrees-of-freedom parallel + serial type hybrid mechanisms containing parallel mec hanism with high coupling motions. *Journal of Mechanisms and Robotics*, 16(2):024501, 2024. doi: 10.1115/1.4056673.

[19] O. Altuzarra, M. Urizar, M. Cichella, and V. Petuya. Kinematic analysis of three degrees of freedom planar parallel continuum mechanisms. *Mechanism and Machine Theory*, 185:105322, 2023. doi: 10.1016/j.mechmachtheory.2023.105311.

[20] J. Li, J. Wang, H. Zhao, et al. Analysis of key technology of lower limb rehabilitation training robot. *Mechanical Design and Manufacturing*, 271(09):220–223, 2013. doi: 10.19356/j.cnki.1001-3997.2013.09.067. (in Chinese).

[21] Z.-W. Zhu, C.-X. Tang, L.-J. Xu, et al. Gait planning and kinematic simulation of a lower limb exoskeleton rehabilitation robot for stroke patients. *Mechanical Design and Manufacturing*, 371(01):247–250+256, 2022. doi: 10.19356/j.cnki.1001-3997.20211123.006. (in Chinese).

[22] Yang Liu. *System of singular nonlinear equations and solution of nonlinear least squares problems*. Xiangtan University, 2003. (in Chinese).

[23] C. Han, K. Yang, T. Chen, et al. Variable stiffness characteristics of a rope-driven ankle rehabilitation robot. *Machine Design and Research*, 38(1):43–50, 2022. doi: 10.13952/j.cnki.jofmdr.2022.0058. (in Chinese).

[24] X. Liu, Y. Qiu, and Y. Sheng. Variable stiffness characteristics of a rope-driven ankle rehabilitation robot. *Journal of Mechanical Engineering*, 47(3):28–35, 2011. (in Chinese).

[25] R. Verhoeven. *Analysis of the Workspace of Tendon-based Stewart Platforms*. Ph.D. Thesis, Duisburg, Gerhard Mercator University, Germany, 2004.

[26] W. Li, C. Su, and J.N. Ye. Analysis of dynamic workspace for under-constrained coordinate suspending system with multi-robot. *Journal of Shanghai Jiaotong University*, 49(10):1916–1923, 2019. doi: 10.16183/j.cnki.jsjtu.2019.02.014. (in Chinese).

[27] A. Pott. Classification and architecture. Chapter 2. In: A. Pot Cable-Driven Parallel Robots. Springer, 2018.